Water Research 208 (2022) 117875

Contents lists available at ScienceDirect

Water Research

journal homepage: www.elsevier.com/locate/watres

Photochemistry of dissolved organic matter in water from the Pearl river (China): Seasonal patterns and predictive modelling

Zhiyang Liao [a], Yi Wang [a], Kunting Xie [a], Nangeng Xie [a], Xixi Cai [a], Lihua Zhou [b], Yong Yuan [a,*]

[a] Guangdong Key Laboratory of Environmental Catalysis and Health Risk Control, School of Environmental Science and Engineering, Institute of Environmental Health and Pollution Control, Guangdong University of Technology, Guangzhou 510006, PR China
[b] School of Biomedical and Pharmaceutical Sciences, Guangdong University of Technology, Guangzhou, 510006, PR China

ARTICLE INFO

Keywords:
Dissolved organic matter
Seasonal variation
Photochemically produced reactive intermediates
Optical properties
Urbanized river

ABSTRACT

Photochemical properties of dissolved organic matter (DOM) vary widely in natural and engineered water systems due to the different dominant compositions. However, seasonal patterns of DOM photochemical properties in urban rivers remain unclear. In this study, two seasons (wet and dry) of water samples were collected from eleven sites throughout the Pearl River (China) to investigate the spatiotemporal variability of DOM optical and photochemical properties. The optical properties of DOM in the Pearl River were characterized by UV–vis and fluorescence spectroscopies, which showed the substantial decrease in absorption coefficient and fluorescence intensity and increase in absorbence ratio (E_2/E_3) and specific absorption coefficient (SUVA) from the wet to dry season. The photochemical properties in terms of the apparent quantum yields of ^{3}DOM*, $^1O_2$ and ·OH from DOM (Φ^3_{DOM}*, Φ^1_{O2} and $\Phi_{\cdot OH,\ DOM}$) under illumination also displayed a significant decrease from the wet to the dry season. Spearman's rank correlation analysis revealed the strongest relationships between Φ^3_{DOM}*, Φ^1_{O2} and $\Phi_{\cdot OH,\ DOM}$ and the relative abundance of microbial humic-like component (C2%) derived from parallel factor analysis (PARAFAC). Partial least squares regression (PLSR) modelling exhibited an excellent prediction strength for steady-state concentrations of $^1O_2$ ($[^1O_2]_{ss}$) and ·OH ($[\cdot OH]_{ss}$) with adjusted R^2 values of 0.85 and 0.91, respectively, by using DOC concentration ([DOC]), optical properties, nitrate and nitrite concentrations as the response variables. In addition, the model identified that the F_{max} of humic-like component C4 ($F_{max\text{-}C4}$) was the most effective predictor amongst the used response variables. This study provides an approach to describe and predict the seasonal patterns of DOM photochemical properties in urbanized rivers, offering a good understanding of the formation mechanism of reactive species from river DOM.

1. Introduction

Dissolved organic matter (DOM) represents a significant and abundant pool of organic carbon that is ubiquitous in aquatic environments and derived from various origins, e.g., terrestrial and microbial sources (Murphy et al., 2008). DOM plays multifaceted roles in biogeochemical processes, including aquatic carbon and nutrient cycling (Coble, 2007; Fu et al., 2007), microbial metabolism (Bai et al., 2017) and trace-metal speciation and transport (Yamashita and Jaffé, 2008). Of great importance are sunlight-driven photochemical processes, wherein chromophoric dissolved organic matter (CDOM) is capable of absorbing sunlight in the upper surface layer of water bodies and forming reactive species called photochemically produced reactive intermediates (PPRIs), such as excited triplet states of DOM (^{3}DOM*), singlet oxygen ($^1O_2$) and hydroxyl radicals (·OH) (Haag et al., 1984; Haag and Hoigné, 1985; Canonica and Freiburghaus, 2001). Characterized by strong reactive properties, these PPRIs can take part in the degradation of many organic contaminants or be quenched by DOM, thereby affecting their fate or the transformation of DOM itself (Zeng and Arnold, 2013; Niu et al., 2014).

The ability to produce PPRIs by irradiated DOM can be evaluated by the apparent quantum yield of PPRIs (Φ_{PPRIs}) (De Laurentiis et al., 2013; McKay et al., 2017). The Φ_{PPRIs} can be further used to estimate the steady-state concentration of PPRIs based on local irradiation conditions and to predict the indirect photodegradation half-life of contaminants combined with second-order rate constants for reactions between PPRIs and contaminants (Peterson et al., 2012; Zeng and Arnold, 2013; McCabe and Arnold, 2016). Previous reports on Φ_{PPRIs} in different water

---

* Corresponding author.
E-mail address: yuanyong@soil.gd.cn (Y. Yuan).

https://doi.org/10.1016/j.watres.2021.117875
Received 4 August 2021; Received in revised form 12 November 2021; Accepted 14 November 2021

bodies demonstrated that the apparent quantum yield of $^3DOM^*$ and $^1O_2$ (Φ^3_{DOM}*and Φ^1_{O2}) both ranged from 10^{-2} to 10^{-3} mol mol-photons^{-1} and that the apparent quantum yield of ·OH ($\Phi_{\cdot OH}$) ranged from 10^{-3} to 10^{-6} mol mol-photons^{-1} (Wasswa et al., 2020). The order of magnitude difference in the yields of various PPRIs is related to their intrinsic formation mechanisms and pathways (Berg et al., 2019). To date, numerous studies have found that Φ_{PPRIs} is highly dependant on the sources, compositions and optical properties of DOM and therefore varies widely in natural and engineered water systems (Berg et al., 2019; Bodhipaksha et al., 2015). Previous findings demonstrated that autochthonous DOM especially effluent organic matter (EfOM) possesses higher Φ_{PPRIs} and higher reactivity than terrestrial DOM (Zhou et al., 2019; Bahnmüller et al., 2014; Dong and Rosario-Ortiz, 2012; Zhang et al., 2014). In addition, a higher aromatic content in DOM suggests a higher production rate of $^3DOM^*$ and $^1O_2$ but a lower Φ^3_{DOM}* and Φ^1_{O2} (McKay et al., 2017; Maizel et al., 2017). On the other hand, Φ_{PPRIs} is positively correlated with the DOM molecular weight surrogate of the absorbence ratio (e.g., $A_{250}/A_{365} = E_2/E_3$), indicating high photoreactivity at low molecular weights (high E_2/E_3) (Maizel and Remucal, 2017b; Lee et al., 2013; McCabe and Arnold, 2016). However, the correlations are weaker and vary with different compositions of DOM when studies cover diverse waters (Mostafa and Rosario-Ortiz, 2013; Maizel and Remucal, 2017a). In general, the complexity of DOM characteristics and composition makes it a challenge to describe the photochemical properties in diverse water systems.

The complex composition of DOM in aquatic environments is attributed to the sensitivity to local hydrogeochemical variations and regional climatic changes (Sulzberger and Arey, 2016; Avagyan et al., 2016). For instance, seasonal variation leads to abundant terrestrial inputs during wet seasons and relatively strong in situ degradation in the dry season (Ni et al., 2020), which significantly alters the composition and characteristics of DOM and thus the photochemical properties (Spencer et al., 2008). Based on this, several studies have focused on the seasonal patterns of DOM photochemical properties in some aquatic ecosystems, such as wetlands and lakes (McCabe and Arnold, 2016; Peterson et al., 2012). However, little attention has been given to the seasonal patterns of DOM photochemical properties in rivers that can be also strongly influenced by seasonal variation. The inherent DOM properties that affect seasonal changes in photochemical characteristics are currently unknown.

In the present study, seasonal surface water samples were collected along the Pearl River, China. The Pearl River chosen here was characterized by sufficient sunlight exposure and distinct seasonal discharge, where the wet season from April to September contributed 80% of the annual discharge volume (Hong et al., 2005). Additionally, the Pearl River flows through the urban area of Guangzhou City and receives effluents from three waste water treatment plants (WWTPs), indicating a strong anthropogenic impact (Meng et al., 2013) and the possibly different photoreactivity from natural rivers. The objectives of this study were thus (i) to characterize the seasonal patterns of the Pearl River water chemistry and riverine DOM optical properties with absorption and fluorescence spectra; (ii) to characterize the seasonal variability of DOM photochemical properties in terms of measuring the apparent quantum yields and steady-state concentrations of $^3DOM^*$, $^1O_2$ and ·OH in the water of the Pearl River; and (iii) to predict the apparent quantum yields or steady-state concentrations of $^3DOM^*$, $^1O_2$ and ·OH based on DOM optical properties and reveal the most effective predictors.

2. Materials and methods

2.1. Sample collection and water chemistry measurement

The Pearl River in this study is referred to as a 96 km-long river that flows through the urban area of the Guangzhou City to the estuary. Eleven sampling sites were chosen along the Pearl River from upstream to downstream (Fig. 1). Site S1 located down by the convergence amongst the Baini River, Xinan River and Liuxi River, where it was less affected by human activity and considered as upstream in this study. Sites from S2 to S8 located in the urbanized and populated area, which were all considered as the urban area sites. Sites S9, S10 and S11 located in the estuary close to the South Sea of China, which were all considered as the downstream sites. Sample collection was conducted in the wet season (August, 2020) and dry season (December, 2020) to explore the temporal and spatial variations in the DOM optical and photochemical properties in the Pearl River. For each sampling site, triplicate surface water samples were collected at 30 cm below the water surface and then mixed together and preserved in pre-acid-washed 1 L high-density polyethylene (HDPE) bottles. Note that sampling on rainy days in the wet season was avoided to minimize the impact of rainfall on the water quality. All of the samples were kept in a cooler with ice inside and transported to the laboratory within 12 h. After arrival at the laboratory, the collected samples were vacuum-filtered through 0.22 μm polyethersulfone membranes and stored in the dark at 4 °C. The chemical analysis, spectral measurement and photochemical experiments were conducted within one week, and no obvious decrease of DOC concentration was observed for the duration of the study. The pH was measured using a pH metre (ST3100, OHAUS) after calibration. Anion (chloride, sulfate, nitrate, nitrite and bromide) concentrations were determined by an ion chromatograph (882 Compact, Metrohm). The concentrations of total dissolved carbon (TC), dissolved organic carbon (DOC) and dissolved inorganic carbon (IC) were quantified in duplicate by a TOC analyser (TOC-L, Shimadzu). The measured water chemistry data are summarized in Table S1 in the supplementary information.

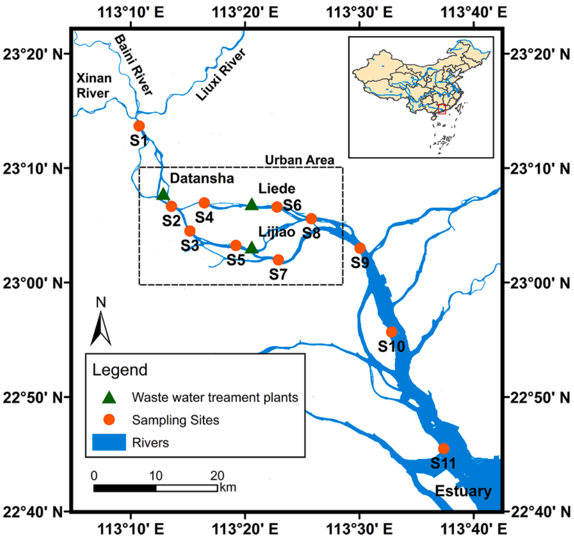

Fig. 1. Map of sampling sites along the Pearl River.

2.2. Ultraviolet-visible absorption spectral analysis and spectral parameter calculation

Ultraviolet-visible absorption spectra were measured from spectrophotometer (UV2600, Shimadzu) using 1-cm quartz cuvettes with a scanning range of 200–800 nm and increments of 1 nm. Ultrapure water was used as both a reference and a blank. The absorption spectral parameters including absorption coefficients (a_{254}, a_{280} and a_{354}), specific UV absorption coefficients ($SUVA_{254}$, $SUVA_{280}$ and $SUVA_{350}$), the absorption coefficients ratio (E_2/E_3), spectral slope coefficients ($S_{275-295}$, $S_{350-400}$ and $S_{290-350}$) and the slope ratio (S_R) were calculated. The detailed calculations and corresponding DOM characterizations and results are shown in Table S2 and S3 in the supplementary information.

2.3. Excitation-emission matrix (EEM) fluorescence spectra measurements and parallel factor analysis (PARAFAC) modelling

The EEM fluorescence spectra of the samples were taken using a fluorescence spectrometer (FLS1000, Edinburgh) in 1-cm quartz cuvettes with excitation wavelengths ranging from 220 to 500 nm and emission wavelengths ranging from 250 to 550 nm in 5-nm intervals. Rayleigh and Raman scattering regions were eliminated and replaced by the interpolation method used in Bahram et al (2006). Then, the matrices were corrected for inner filter effects, blank subtracted with ultrapure water and normalized by the Raman peak area of water at an excitation wavelength of 350 nm. Fluorescence spectral parameters, including the fluorescence index (FI), biological index (BIX) and humification index (HIX), were calculated to distinguish the composition and properties of DOM. The detailed calculations and explanation and results are shown in Table S2 and S3.

Parallel factor analysis (PARAFAC) is an alternating least squares algorithm that decomposes EEM data signals into a set of trilinear terms and a residual array (Murphy et al., 2013). Before the analysis, measurements at excitation wavelengths below 250 nm were excluded from the corrected data to minimize unreliable model output (Murphy et al., 2011). A total of 22 EEMs of the water samples from two seasons were subjected to PARAFAC analysis. The PARAFAC models with 2–6 components were both calculated for all EEMs, while Ex and Em loadings of PARAFAC components were constrained to non-negative values. Considering the small dataset in this study, diagnostic tools of residual analysis and random initialization were adopted to determine the appropriate number of PARAFAC components (Stedmon and Bro, 2008). The result of PARAFAC modelling was matched with components of similar shape and location obtained in other published studies in the OpenFluor online dataset (Murphy et al., 2014).

2.4. Photochemical Experiments

All photochemical experiments were performed in a photochemical reaction apparatus (CEL-LAX500, Beijing China Education Au-light Co., Ltd), in which a 500 W xenon lamp was applied as a simulated sunlight source with a 290-nm cut-off filter. The filtered spectrum of the lamp is given in Fig. S1. The photon irradiance in solution (8.10×10^{-6} Einstein L^{-1} s^{-1}) was determined using the *p*-nitroanisole/pyridine (PNA/pyr) actinometer method Laszakovits et al (2017), which was further used to calculate the rate of light absorption (Ra, Einstein L^{-1} s^{-1}) for each water sample.

The photochemical properties of the water samples were assessed by measuring the PPRIs with specific probe compounds, including 2, 4, 6-trimethylphenol (TMP) as an electron transfer probe for $^3DOM^*$ (Canonica and Freiburghaus, 2001), furfuryl alcohol (FFA) for $^1O_2$ (Haag et al., 1984) and terephthalic acid (TPA) for ·OH and lower-energy hydroxylating species (Page et al., 2010; Page et al., 2011). River water samples (20 mL aliquots) were spiked with different probes that were both at an initial concentration of 1 mM and placed into quartz test tubes in a merry-go-round sample holder that rotated around the lamp. The tubes were irradiated for 4 h at room temperature and magnetically stirred during irradiation, with subsamples withdrawn over time for analysis. Lamp radiation was vertically incident over the solutions, and the optical path length was approximately 2.0 cm. Duplicate or triplicate measurements were performed for each irradiation experiment. The concentrations of TMP, FFA and generated 2-hydroxyterephthalic acid (hTPA) after irradiation were measured via HPLC (Essentia LC-16, Shimadzu) using the method described in Table S4. The direct photolysis of TMP and FFA, as well as hTPA formation from TPA, were also measured upon irradiation in ultrapure water as a blank. The apparent quantum yields, formation rates and steady-state concentrations of PPRIs were calculated as detailed in the supplementary information.

2.5. Statistical Analysis

Significance differences in the water chemistry, DOM optical indices (absorption and fluorescence spectral parameters and specific PARAFAC component and the relative ratio) and DOM photochemical properties between the samples from the two seasons were tested using a nonparametric Mann-Whitney U test. Spearman's rank correlation analysis was conducted to identify statistically significant bivariate trends between apparent quantum yields of the PPRIs and the bulk DOM properties (bulk DOC concentrations and DOM optical indices). A Spearman's correlation coefficient (ρ) greater than 0.6 or less than -0.6 was considered to be strongly correlated. All the statistical analyses above were performed in SPSS Statistic 25 (IBM). Partial least squares regression (PLSR) was performed using SIMCA 14.1 (Umetrics) to explore the predictive strength of bulk DOM properties and the concentrations of nitrate and nitrite for the overall DOM photochemical properties (i.e., steady-state concentrations and apparent quantum yields of PPRIs) of the two seasons of water samples. Due to the robustness to the collinearity of multiple variables, the PLSR model could identify an optimal set of orthogonal principal components from the dataset and maximize the variability explanation between the predictor and response variables (Wold et al., 2001). Cross validation was applied to prevent overfitting of the model. Each predictor variable was ranked according to its relevance in explaining the variable importance in the projection (VIP) score of the response variables, with a VIP score greater than 1.0 being the most influential (Kothawala et al., 2014).

3. Results

3.1. Characterization of river water chemistry

The measured water chemistry of the two seasonal samples is presented in Table S1. The average pH increased from the wet to the dry season ($p < 0.01$). The mean anion concentrations of Cl^-, SO_4^{2-} and Br^- substantially increased by 26, 4 and 27 times from the wet to the dry season, respectively. Additionally, dramatically high of Cl^-, SO_4^{2-} and Br^- concentrations in the downstream area (S9-S11) in the dry season were observed. The average nitrate concentration significantly increased by 45% from the wet to the dry season ($p < 0.01$), while the average nitrite concentration varied little between the two seasons ($p > 0.05$). The nitrate and nitrite concentrations in the urban area (S2-S8) were higher than those in the downstream area (S9-S11) in both two seasons. In addition, the average [DOC] decreased by 34% from the wet to the dry season. The results of the seasonal variability of river water chemistry are further provided in the supplementary information.

3.2. Characterization of DOM optical properties

Box charts of the absorption and fluorescence spectral parameters are shown in Fig. 2 and Fig. S2. For absorption spectral parameters, the mean values for absorption coefficients of a_{254} and a_{280} both decreased by 17% from the wet to the dry season ($p < 0.05$), while the mean value for a_{350} decreased little ($p > 0.05$). In contrast, the mean value for $SUVA_{350}$ significantly increased by 32% from the wet to the dry season ($p < 0.01$), while the mean values for $SUVA_{254}$ and $SUVA_{280}$ insignificantly increased ($p > 0.05$). The mean values for the spectral slopes of $S_{350–400}$ and $S_{290–350}$ were significantly higher in the dry season than in the wet season ($p < 0.05$), but the seasonal difference in the average $S_{275–295}$ was small and statistically insignificant ($p > 0.05$). The increase in the average value for E_2/E_3 from the wet to the dry season was found to be significant ($p < 0.05$). The mean value for the slope ratio of S_R decreased little ($p > 0.05$). For fluorescence spectral parameters, the mean value for FI was relatively unchanged between seasons ($p > 0.05$). Significantly high BIX mean values and low HIX mean values were observed in the dry season ($p < 0.05$). In addition, higher BIX values were observed in the urban area than in the downstream area in both

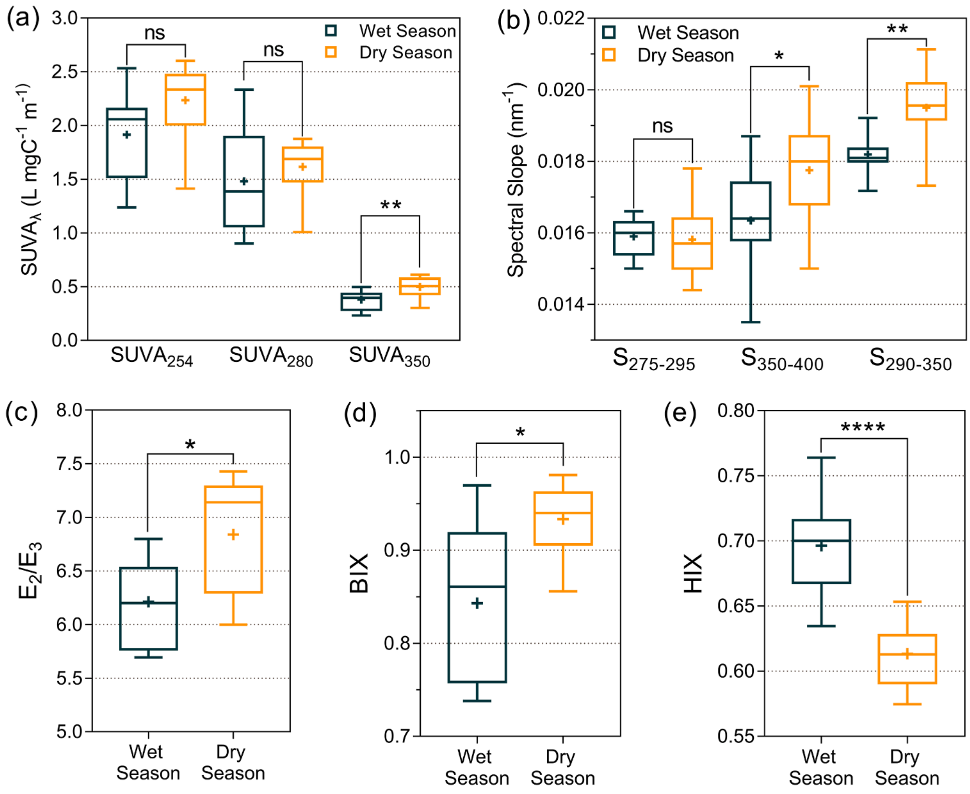

Fig. 2. Box-and-whisker plots of the seasonal (a) specific ultraviolet absorption coefficients (SUVA) at 254, 280 and 350 nm; (b) spectral slope (S) in the wavelength ranges of 275–295, 350–400 and 290–350 nm; (c) the ratio of the absorbence at 250 nm to the absorbence at 365 nm (E_2/E_3); (d) biological index (BIX), the interval description of BIX was as follows (Huguet et al., 2009): BIX < 0.8 (less fresh DOM), 0.8 < BIX < 1 (more fresh DOM) and BIX > 1 (autochthonous DOM); (e) humification index (HIX). The boxes represent the interquartile ranges. The whiskers represent the minimum and the maximum values. The centreline in each box represents the median, while the plus sign "+" represents the mean. Significant differences between two seasons are denoted by "*" ($p < 0.05$), "**" ($p < 0.01$), "***" ($p < 0.001$) or "****" ($p < 0.0001$). "ns" represents that there is no statistically significant difference.

seasons (Table S3).

A 6-component model was determined from PARAFAC analysis (Fig. S3). The components were identified and matched in the online OpenFluor database depository (95% minimum similarity score; Murphy et al., 2014), including C1 (terrestrial humic-like, peak A), C2 (microbial humic-like, peak M), C3 (tryptophan-like, peak T), C4 (terrestrial humic-like, peak C), C5 (terrestrial humic-like, peak D) and C6 (tyrosine-like, peak B). The descriptions and locations of the PARAFAC components of DOM are summarized in Table S5. The fluorescence intensity (F_{max}) and the relative abundance of the fluorescent components for each sampling site are plotted in Fig. S4. The sum of the F_{max} of all components (F_T) of each sample decreased along the Pearl River, with little change in the relative abundance of each component. For the average level for each season (Fig. 3), a substantial decline of 40% in the F_T from the wet season to the dry season was observed. In addition, the F_{max} of the fluorescence components except C3 decreased greatly from the wet to the dry season and followed the order C2 (51%) > C5 (50%) > C1 (46%) > C6 (44%) > C4 (41%). amongst the components, C1 dominated the fluorescence composition and accounted for 35% and 32% of the average F_T in the wet and dry seasons, respectively. On the other hand, although the average value for F_{max} of C3 ($F_{max\text{-}C3}$) varied little, an increase in the average relative abundance of C3 (C3%) from 13% to 24% was observed between the two seasons. The component ratio was further applied to simulate the commonly used peak ratio to study the relative changes in the components (Fig. S5 and Table S2). The C1/C3 and C4/C3 (i.e., A/T and C/T) ratios decreased by 52% and 47% from the wet to the dry season, respectively, while the C4/C1 and C4/C2 (i.e., C/A and C/M) ratios slightly increased.

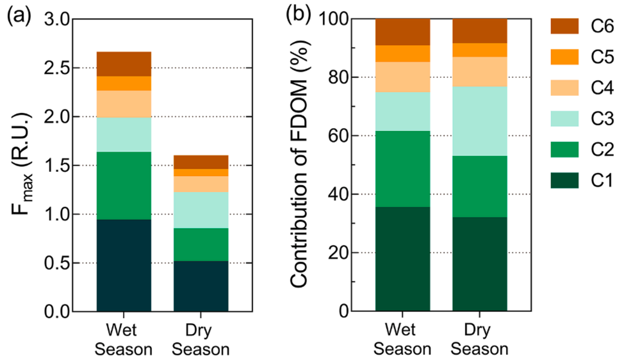

Fig. 3. The average (a) fluorescence intensity (F_{max}) and (b) relative abundance of each PARAFAC component in the two seasons.

3.3. Photoreactivity of river water samples from the Pearl river

The calculated apparent quantum yields, formation rates and steady-state concentrations of PPRIs are shown in Fig. 4a-d, Fig. S6 and Table S6. The $\Phi_{^3DOM^*}$ and $\Phi_{^1O_2}$ of all samples were in the range of 0.54–2.20 × 10^{-2} mol mol-photons^{-1} and 0.88–4.56 × 10^{-2} mol mol-photons^{-1} and the mean values were 1.21 ± 0.40 × 10^{-2} mol mol-photons^{-1} and 2.52 ± 1.20 × 10^{-2} mol mol-photons^{-1}. On the other hand, the measured $\Phi_{\cdot OH}$ (including the contribution of DOM and photolysis of nitrate and nitrite) for all samples ranged from 2.84 × 10^{-4} to 5.23 × 10^{-4} mol mol-photons^{-1} with a mean value of 4.15 ± 0.67 × 10^{-4} mol mol-photons^{-1}. The contributions of the photolysis of nitrate and nitrite were quantified with the results depicted in Fig. S7 and Table S7. The normalized ·OH formation rates for nitrate and nitrite were calculated to be 1.32 × 10^{-7} M s^{-1} $M_{NO3\text{-}}^{-1}$ and 1.79 × 10^{-6} M s^{-1} $M_{NO2\text{-}}^{-1}$, respectively (Fig. S7). The contribution of nitrate and nitrite photolysis based on the concentrations was in the range of 24.3–65.5%, with a mean value of 48.8 ± 13.8% (Table S7). Additionally, the ·OH formation rate from DOM ($R_{\cdot OH,\ DOM}$) was obtained after subtracting the contributions of nitrate and nitrite from the overall formation ($R_{\cdot OH}$). The apparent quantum yield of ·OH from DOM ($\Phi_{\cdot OH,\ DOM}$) was further calculated by the obtained $R_{\cdot OH,\ DOM}$. The mean value for $\Phi_{\cdot OH,\ DOM}$ (including only the contribution of DOM) was 2.17 ± 0.64 × 10^{-4} mol mol-photons^{-1} with a range of 1.18 × 10^{-4} to 3.41 × 10^{-4} mol mol-

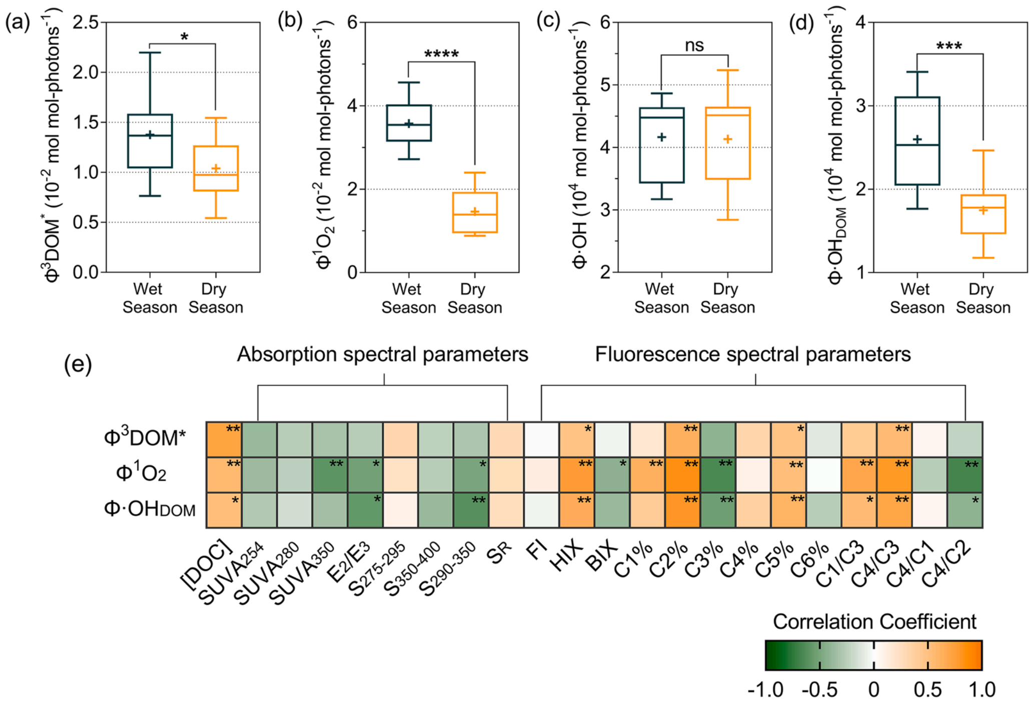

Fig. 4. Box-and-whisker plots of the seasonal apparent quantum yields of PPRIs: (a) $\Phi^{3}{}_{DOM}*$; (b) $\Phi^{1}{}_{O_2}$; (c) $\Phi_{\cdot OH}$ and (d) $\Phi_{\cdot OH,\ DOM}$. The boxes represent the interquartile ranges. The whiskers represent the minimum and the maximum values. The centreline in each box represents the median, while the plus sign "+" represents the mean. Significant differences between two seasons are denoted by "*" ($p < 0.05$), "**" ($p < 0.01$), "***" ($p < 0.001$) or "****" ($p < 0.0001$). "ns" represents that there is no statistically significant difference. (e) Spearman's rank correlations between apparent quantum yields of $^{3}DOM*$, $^{1}O_2$ and $\cdot OH_{DOM}$ and bulk DOM properties in the two seasons. Significant correlations are denoted by "*" ($p < 0.05$) or "**" ($p < 0.01$).

photons^{-1}. The average apparent quantum yields for all PPRIs except $\Phi_{\cdot OH}$ significantly decreased by 39% from the wet to the dry season. amongst them, $\Phi^{1}{}_{O2}$ decreased the most, by 59%, from the wet to the dry season. $\Phi^{3}{}_{DOM}*$ and $\Phi_{\cdot OH,\ DOM}$ decreased by 25% and 33% from the wet to the dry season, respectively. No obvious differences between the urban and downstream areas were found in terms of $\Phi^{3}{}_{DOM}*$, $\Phi^{1}{}_{O2}$ and $\Phi_{\cdot OH,\ DOM}$, while a general decrease in $\Phi_{\cdot OH}$ along the Pearl River in both seasons was observed.

3.4. Correlations between ΦPPRIs and bulk DOM properties

The correlations between the Φ_{PPRIs} ($\Phi^{3}{}_{DOM}*$, $\Phi^{1}{}_{O2}$ and $\Phi_{\cdot OH,\ DOM}$)

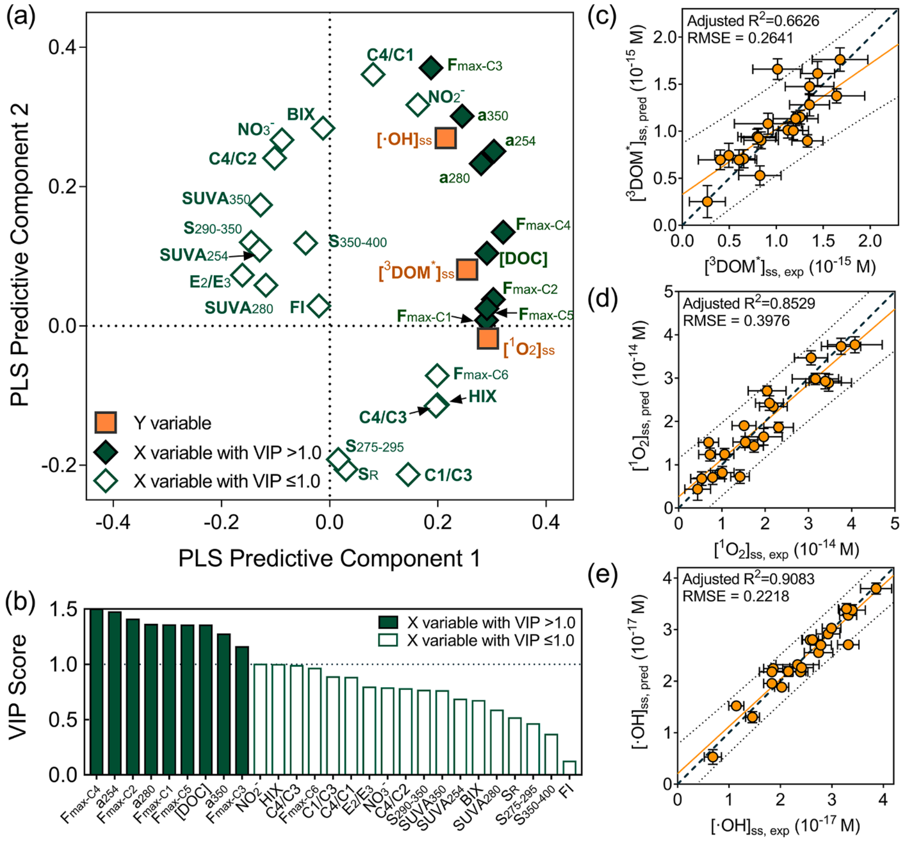

Fig. 5. Partial least squared regression (PLSR) modelling of steady-state concentrations of $^{3}DOM*$, $^{1}O_2$ and $\cdot OH$ (n=22): (a) loading scatter plots of the PLS analysis where the Y variable ($[^{3}DOM*]_{ss}$, $[^{1}O_2]_{ss}$ and $[\cdot OH]_{ss}$) is the response variable, the X variable is the predictor variable, and VIP is the variable influence on projection; (b) the VIP score plot of predictor variables where the dotted line represents a VIP score threshold of 1.0 (X variables with a VIP score of > 1.0 were the most important for model performance); (c-e) cross plots of experimentally measured $[^{3}DOM*]_{ss}$, $[^{1}O_2]_{ss}$ and $[\cdot OH]_{ss}$ versus $[^{3}DOM*]_{ss}$, $[^{1}O_2]_{ss}$ and $[\cdot OH]_{ss}$ as predicted by two PLS predictive components. Error bars indicate one standard deviation of duplicate or triplicate measurements for experimentally determined $[PPRIs]_{ss,exp}$ or the 95% confidence interval for the predicted $[PPRIs]_{ss,pred}$. The blue dashed line represents the 1:1 ratio and the upper and lower dotted lines represent the 95% prediction interval of the best-fit orange solid line.

and bulk DOM properties of water samples were explored in the two seasons (Fig. 4e). $\Phi^1{}_{O2}$ and $\Phi_{\cdot OH,\ DOM}$ had strong correlations with most of the bulk DOM property indicators, while $\Phi^3{}_{DOM}*$ correlated strongly with few indicators. $\Phi^3{}_{DOM}*$, $\Phi^1{}_{O2}$ and $\Phi_{\cdot OH,\ DOM}$ correlated positively with [DOC], HIX, C2%, C5% and C4/C3, with the average Spearman's rank coefficients following the order C2% (0.75) > C4/C3 (0.67) > [DOC] (0.65) > HIX (0.62) > C5% (0.53) ($p < 0.05$). However, indicators of DOM aromaticity (SUVAs) and DOM molecular weight (E_2/E_3) or spectral slopes showed negative and relatively weak correlations with Φ_{PPRIs}. amongst all the bulk DOM property indicators, $\Phi^3{}_{DOM}*$ had the strongest positive correlation with [DOC], where Spearman's rank coefficient was 0.71 ($p < 0.01$). Both $\Phi^1{}_{O2}$ and $\Phi_{\cdot OH,\ DOM}$ had the strongest correlation with C2% with Spearman's rank coefficients of 0.83 and 0.80 ($p < 0.01$), respectively.

3.5. PLSR modelling of the DOM photoreactivity in Pearl River water

PLSR modelling was applied utilizing the steady-state concentration of PPRIs ($[PPRIs]_{ss}$) as the response variable and the bulk DOM properties and the concentrations of nitrate and nitrite of the river samples as predictor variables and the results are shown in Fig. 5 and Table S8. Overall, the PLSR model extracted two predictive components from $[^3DOM^*]_{ss}$, $[^1O_2]_{ss}$ and $[\cdot OH]_{ss}$ by using 27 predictor variables (Table S8). The average explained fraction of the variation in $[PPRIs]_{ss}$ after cross validation (Q^2) for this model was 0.77. The apparent quantum yields of PPRIs were also predicted by PLSR modelling, but the prediction accuracy was relatively lower ($Q^2 = 0.49$) by the selected predictors (Fig. S8 and Table S9). The adjusted R^2 in $[PPRIs]_{ss}$ followed the pattern of $[\cdot OH]_{ss}$ (0.91) > $[^1O_2]_{ss}$ (0.85) > $[^3DOM^*]_{ss}$ (0.66).

On the loading scatter plot (Fig. 5a), $[^3DOM^*]_{ss}$ and $[^1O_2]_{ss}$ clustered tightly and were situated near positive indicators of [DOC] and the PARAFAC components, except $F_{max\text{-}C3}$ and $F_{max\text{-}C6}$ on the axis of predictive component 1, but were located opposite to negatively influential predictors of the aromaticity and molecular weight indicators. $[^3DOM^*]_{ss}$ and $[^1O_2]_{ss}$ exhibited limited separation on the second component axis. On the other hand, $[\cdot OH]_{ss}$ was well separated from $[^3DOM^*]_{ss}$ and $[^1O_2]_{ss}$ along the axis of predictive component 2 and clustered close to the nitrite concentration and absorption coefficients. The VIP scores of 9 predictors were greater than 1 and followed the order $F_{max\text{-}C4} > a_{254} > F_{max\text{-}C2} > a_{280} > F_{max\text{-}C1} > F_{max\text{-}C5} > [DOC] > a_{350} > F_{max\text{-}C3}$.

4. Discussion

4.1. Difference in DOM optical properties between two seasons

The measured absorption spectral parameters indicated the characteristics of DOM in the Pearl River in the two seasons. Overall, DOM in the Pearl River presented relatively low aromaticity and molecular weight, which were indicated by the low average SUVA ($SUVA_{254}$: 2.07 ± 0.41 L mgC^{-1} m^{-1}; $SUVA_{280}$: 1.55 ± 0.37 L mgC^{-1} m^{-1}) and high average E_2/E_3 (6.53 ± 0.56) (Ni et al., 2020). The general increase in SUVA in the dry season indicated higher DOM aromaticity from the wet to the dry season. Similar variability in SUVA can be found in a previous study (Meng et al., 2013), but with generally higher SUVA levels in the headwater tributaries of the upper Yangtze River in both seasons (Ni et al., 2020). On the other hand, the increase in $S_{350–400}$, $S_{290–350}$ and E_2/E_3 in the dry season suggested a low molecular weight for the DOM in the dry season (Helms et al., 2008). The inconsistency of the seasonal variation of the molecular weight surrogates was possibly due to the complicated composition of DOM and the sensitivity of chromophores with different wavelengths to seasonal variability.

The variation in the fluorescence characteristics well described the DOM source features and compositions in the Pearl River in the two seasons. The relatively unchanged FI between the two seasons suggested comparable contributions from terrestrial and microbial sources (McKnight et al., 2001), which indicated that seasonal variation had little impact on the DOM source features. A significant decrease in HIX and an increase in BIX demonstrated a low degree of humification and a relatively high contribution from recently produced autochthonous DOM in the dry season (Huguet et al., 2009). However, the average relative abundances of autochthonous components (C2%, C3% and C6%) slightly increased from 49% to 54% from the wet to the dry season, demonstrating a limited increase in the contribution of recently produced autochthonous DOM. The possible explanation for the limited contribution might be the inhibited microbial activity at low temperature or the presence of a certain amount of terrestrially derived recalcitrant DOM in the Pearl River in the dry season.

The humic-like components (C1, C2, C4, C5) had a greater F_{max} than the protein-like components (C3 and C6), suggesting that the humic-like substances were important contributors to the fluorescent DOM (FDOM) in the Pearl River. The 40% decrease in the F_{max} of F_T from the wet season to the dry season was slightly higher than the seasonal decline of 34% in the [DOC], which might suggest that FDOM was more sensitive to seasonal variation than the [DOC]. The component ratio was applied to further to study the relative changes in the components. As shown in Fig. S5, the humic-like components had a more rapid seasonal decline than the protein-like components and the microbial humic-like component C2 had the greatest relative variability.

4.2. DOM photoreactivity characterization in the Pearl River water

The measured $\Phi^3{}_{DOM}*$ and $\Phi^1{}_{O2}$ were the same order of magnitude as the values for surface waters (Wasswa et al., 2020), which were slightly higher than those measured for natural rivers ($\Phi^3{}_{DOM}*$: 0.96 × 10^{-2} mol mol-photons^{-1}, $\Phi^1{}_{O2}$: 2.35 × 10^{-2} mol mol-photons^{-1}) (Chen et al., 2020) but were lower than those measured for effluent-dominated rivers ($\Phi^3{}_{DOM}*$: 3.53 × 10^{-2} mol mol-photons^{-1}, $\Phi^1{}_{O2}$: 5.02 × 10^{-2} mol mol-photons^{-1}) (O'Connor et al., 2019). A poor correlation between $\Phi^3{}_{DOM}*$ and $\Phi^1{}_{O2}$ was observed ($\rho = 0.39$, $p = 0.07$), indicating that a low overlap existed in the triplet states based on triplet-state-induced electron transfer and energy transfer reactions of the DOM in the Pearl River. On the other hand, the measured $\Phi_{\cdot OH}$ was an order of magnitude higher than those reported for other aquatic environments (Wasswa et al., 2020; McCabe and Arnold, 2016). Due to the relatively high concentrations of nitrate and nitrite observed in this study, the measured hydroxyl radical formation rates ($R_{\cdot OH}$) and $\Phi_{\cdot OH}$ included necessary contributions from the photolysis of nitrate and nitrite (Vione et al., 2006). As shown in Fig. S7, the normalized ·OH formation rates for nitrate and nitrite obtained were slightly lower than the previously reported values of 1.7 × 10^{-7} M s^{-1} $M_{NO3\text{-}}{}^{-1}$ for nitrate and 5.08 × 10^{-6} M s^{-1} $M_{NO2\text{-}}{}^{-1}$ for nitrite (Vione et al., 2006; Xu et al., 2020), partially due to the different irradiation intensities and probes. The calculated contribution of nitrate and nitrite photolysis to ·OH formation was comparable to that of DOM (Table S7), indicating that nitrate and nitrite were also important sources of ·OH in the Pearl River, especially in the urban area. The calculated $\Phi_{\cdot OH,\ DOM}$ was the same order of magnitude as $\Phi_{\cdot OH}$ and compared well with values determined for Antarctic lakes (2.07 × 10^{-4} mol mol-photons^{-1}), the St. Louis River (2.25 × 10^{-4} mol mol-photons^{-1}) and WWTP effluent (2.54 × 10^{-4} mol mol-photons^{-1}) (De Laurentiis et al., 2013; Berg et al., 2019; Lee et al., 2013). Note that a significant relationship between $\Phi^3{}_{DOM}*$ and $\Phi_{\cdot OH,\ DOM}$ was observed ($\rho = 0.54$, $p < 0.01$), which might imply that $^3DOM^*$ was the precursor of ·OH and involved in ·OH production, possibly via O_2 reduction or H atom abstraction from water (Sharpless and Blough, 2014; Page et al., 2011). In general, as an urbanized river, the overall photoreactivity of the Pearl River water characterized by apparent quantum yields was higher than that of natural rivers but lower than that of effluent-dominated rivers. In addition, the low $\Phi^3{}_{DOM}*$ and $\Phi^1{}_{O2}$ and seasonally unchanged $\Phi_{\cdot OH}$ in the dry season suggested a lower photoreactivity in the dry season than in the wet season.

4.3. *Strong correlation between fluorescence characteristics and DOM photoreactivity*

Correlation analysis between Φ_{PPRIs} ($\Phi^3{}_{DOM}*$, $\Phi^1{}_{O2}$ and $\Phi_{\cdot OH,\ DOM}$) and the bulk DOM properties was conducted to gain deeper insights into the factors influencing the seasonal variation in the DOM photochemistry in the Pearl River. The DOC concentration and fluorescence spectral parameters (including PARAFAC results) correlated strongly with Φ_{PPRIs}, indicating a better description of seasonal photoreactivity compared with absorption spectral parameters. The parameters of HIX, C2%, C5% and C4/C3 exhibited a strong and positive correlation with Φ_{PPRIs} and similar correlations were found in previous studies (Page et al., 2014; Timko et al., 2014; McKay et al., 2017). These parameters are used as proxies of the content and variation of humic substances to some extent (Hansen et al., 2016), suggesting that the seasonal variability of humic substances significantly affects the formation efficiency of PPRIs in the Pearl River.

The strongest correlations between $\Phi^1{}_{O2}$ and the fluorescence characteristics were observed, wherein the microbial source C2% correlated more strongly with $\Phi^1{}_{O2}$ than those derived from terrestrial sources (C1%, C4% and C5%). Previous studies suggested that microbial-derived CDOM possessed more high-energy triplet states to contribute to the formation of $^1O_2$, leading to a higher $\Phi^1{}_{O2}$ than that from terrestrial-derived CDOM (Zhou et al., 2019; Peterson et al., 2012). Although $\Phi^3{}_{DOM}*$ was less correlated with the bulk DOM properties, the [DOC] and C2% could well describe the seasonal variation. A strong correlation between Φ_{PPRIs} and the molecular weight indicator E_2/E_3 has been reported previously (McCabe and Arnold, 2016; Du et al., 2018), while weak and negative results were observed in this study. One possible explanation for this divergence was that the E_2/E_3 varied in a narrow range (5.69–7.33) compared to that (2.68–9.71) reported by Du et al (2018). In addition, exceptions occurred when the correlations were conducted under a broader set of DOM from diverse sources (Maizel and Remucal, 2017a; Mostafa and Rosario-Ortiz, 2013). More importantly, seasonal variation significantly altered the composition and properties of DOM in the Pearl River, resulting in an insufficient effect from molecular weight changes on Φ_{PPRIs}. In conclusion, the sources and relative changes in humic substances are important in determining PPRI generation efficiency in the Pearl River, with C2% being the most important factor.

4.4. *PPRI steady-state concentration prediction performance by the PLSR model*

Considering that the lifetimes of contaminants in aquatic environments are significantly affected by $[PPRIs]_{ss}$ (Zeng and Arnold, 2013), PLSR modelling was applied to predict the $[PPRIs]_{ss}$ of the river samples. The model exhibited an excellent prediction accuracy (Q^2: 0.77) and greatly described the variation of $[PPRIs]_{ss}$ by the selected variables, performing slightly better than the PLSR prediction of $[PPRIs]_{ss}$ (Q^2: 0.73) that only used the measured EEM (Section 3; Fig. S9 and Table S10). As the VIP scores suggested, the absorption coefficient and fluorescence intensity showed great importance to the model, and $F_{max\text{-}C4}$ most affected the model performance of the predictors with VIP scores greater than 1. On the loading scatter plot, the proximity of $[PPRIs]_{ss}$ to the predictors could generally describe the positive contribution of the predictors to $[PPRIs]_{ss}$. Based on the results, the predictors of [DOC] and the F_{max} of components except C3 and C6 were found to have positive effects on $[^3DOM*]_{ss}$ and $[^1O_2]_{ss}$. The absorption coefficients and nitrite concentration showed positive contributions to $[\cdot OH]_{ss}$. The predictability of the model was higher for $[\cdot OH]_{ss}$ and $[^1O_2]_{ss}$ than for $[^3DOM*]_{ss}$, indicating that the selected predictor variables better described the variability in $^1O_2$ and ·OH concentrations. In addition, the large difference between the predictive strengths of $[^3DOM*]_{ss}$ and $[^1O_2]_{ss}$ implied that the model based on these predictor variables was more likely to explain the energy transfer pathway of ^{3}DOM* rather than the electron transfer pathway. The less unsatisfactory prediction power of $[^3DOM*]_{ss}$ suggested that more characteristics related to the electron transfer pathway of ^{3}DOM* were required to gain additional insights into the factors that dominate the variation in $[^3DOM*]_{ss}$ (Zhou et al., 2019; Maizel and Remucal, 2017a). The combination of the DOM properties and the nitrate and nitrite concentrations in this study exhibited a good prediction of the $[\cdot OH]_{ss}$ in the Pearl River, possibly due to the high apparent quantum yield of ·OH by the photolysis of nitrite (Vione et al., 2014). Overall, the PLSR modelling provided initial insights into the predictors of the seasonal DOM photochemical properties in the Pearl River.

Based on the results of the correlation analysis and PLSR modelling, we found a strong and positive relationship between the fluorescence characteristics of DOM and PPRI formation. The relationships between DOM fluorescence characteristics and PPRI formation are expected, as DOM fluorescence emissions are generated by the release of the energy of excited singlet state DOM (^{1}DOM*) which is the main precursor of ^{3}DOM*. Therefore, a higher fluorescence intensity might be able to indicate higher production of ^{1}DOM*. This assumption is supported by a previous study that explored the effect of heavy metals on DOM photoreactivity by quenching fluorescence to inhibit the formation of ^{1}DOM*, with the results showing that the apparent quantum yields of PPRIs decreased as the quenching effect increased (Wan et al., 2019). Therefore, the concomitant decrease in FDOM and DOM photoreactivity from the wet to the dry season might be explained by the decrease in ^{1}DOM* production leading to the subsequent decline in ^{3}DOM* and downstream PPRIs of $^1O_2$ and ·OH production.

5. Conclusions

In this study, the photochemical and optical properties of DOM in the Pearl River water were characterized to understand its fate and environmental roles. The results showed that DOM in the Pearl River was characterized by low aromaticity and molecular weight indicated by the low $SUVA_{254}$ and high E_2/E_3 values. The levels of $\Phi^3{}_{DOM}*$ and $\Phi^1{}_{O2}$ were between those of natural rivers and effluent-dominated rivers, while $\Phi_{\cdot OH}$ was an order of magnitude higher than those reported for other aquatic environments. Seasonal variation significantly changed the bulk properties of DOM, leading to a subsequent decrease in Φ_{PPRIs}, and amongst which $\Phi^1{}_{O2}$ decreased most by 59% from the wet to the dry season. [DOC], absorption coefficients and fluorescence intensity significantly decreased from the wet to the dry season. Meanwhile, the increase of SUVA and E_2/E_3 indicated the increased DOM aromaticity and decreased DOM molecular weight from the wet to the dry season, respectively. Spearman's correlation analysis indicated that Φ_{PPRIs} strongly correlated with DOM fluorescent characteristics, with C2% being the most important factor. The PLSR model identified the $F_{max\text{-}C4}$ as the most effective predictors of $[PPRIs]_{ss}$ amongst the measured bulk DOM properties, nitrate and nitrite concentrations. The prediction strength of the PLSR model was higher in $[\cdot OH]_{ss}$ and $[^1O_2]_{ss}$ but weaker in $[^3DOM*]_{ss}$. The concomitant decrease of DOM photoreactivity and fluorescence intensity was possibly due to the loss of ^{1}DOM*, which was the main precursors of ^{3}DOM*. Overall, this study provides additional insights into the factors of DOM photochemical variability and a robust prediction of seasonal photoreactivity of river water, which may have important implications for regional contaminant attenuation on a temporal scale.

Declaration of Competing Interest

The authors declare that they have no known competing financial interests or personal relationships that could have appeared to influence the work reported in this paper.

Acknowledgements

This work was supported by National Natural Science Foundation of China (41877045, 21876032, and 41907122) and China Postdoctoral Science Foundation (No. 2021M690728).

Supplementary materials

Supplementary material associated with this article can be found, in the online version, at doi:10.1016/j.watres.2021.117875.

Reference

Avagyan, A., Runkle, B.R.K., Hennings, N., Haupt, H., Virtanen, T., Kutzbach, L., 2016. Dissolved organic matter dynamics during the spring snowmelt at a boreal river valley mire complex in northwest russia. Hydrol. Processes 30 (11), 1727–1741.

Bahnmüller, S., von Gunten, U., Canonica, S., 2014. Sunlight-induced transformation of sulfadiazine and sulfamethoxazole in surface waters and wastewater effluents. Water Res. 57, 183–192.

Bahram, M., Bro, R., Stedmon, C., Afkhami, A., 2006. Handling of rayleigh and raman scatter for parafac modeling of fluorescence data using interpolation. J. Chemom. 20 (3-4), 99–105.

Bai, L., Cao, C., Wang, C., Xu, H., Zhang, H., Slaveykova, V.I., Jiang, H., 2017. Toward quantitative understanding of the bioavailability of dissolved organic matter in freshwater lake during cyanobacteria blooming. Environ. Sci. Technol. 51 (11), 6018–6026.

Berg, S.M., Whiting, Q.T., Herrli, J.A., Winkels, R., Wammer, K.H., Remucal, C.K., 2019. The role of dissolved organic matter composition in determining photochemical reactivity at the molecular level. Environ. Sci. Technol. 53 (20), 11725–11734.

Bodhipaksha, L.C., Sharpless, C.M., Chin, Y.-P., Sander, M., Langston, W.K., MacKay, A. A., 2015. Triplet photochemistry of effluent and natural organic matter in whole water and isolates from effluent-receiving rivers. Environ. Sci. Technol. 49 (6), 3453–3463.

Canonica, S., Freiburghaus, M., 2001. Electron-rich phenols for probing the photochemical reactivity of freshwaters. Environ. Sci. Technol. 35 (4), 690–695.

Chen, Y., Hozalski, R.M., Olmanson, L.G., Page, B.P., Finlay, J.C., Brezonik, P.L., Arnold, W.A., 2020. Prediction of photochemically produced reactive intermediates in surface waters via satellite remote sensing. Environ. Sci. Technol. 54 (11), 6671–6681.

Coble, P.G., 2007. Marine optical biogeochemistry: the chemistry of ocean color. ChemInform 38 (20).

De Laurentiis, E., Buoso, S., Maurino, V., Minero, C., Vione, D., 2013. Optical and photochemical characterization of chromophoric dissolved organic matter from lakes in terra nova bay, antarctica. evidence of considerable photoreactivity in an extreme environment. Environ. Sci. Technol. 47 (24), 14089–14098.

Dong, M.M., Rosario-Ortiz, F.L., 2012. Photochemical formation of hydroxyl radical from effluent organic matter. Environ. Sci. Technol. 46 (7), 3788–3794.

Du, Z., He, Y., Fan, J., Fu, H., Zheng, S., Xu, Z., Qu, X., Kong, A., Zhu, D., 2018. Predicting apparent singlet oxygen quantum yields of dissolved black carbon and humic substances using spectroscopic indices. Chemosphere 194, 405–413.

Fu, P., Wu, F., Liu, C., Wang, F., Li, W., Yue, L., Guo, Q., 2007. Fluorescence characterization of dissolved organic matter in an urban river and its complexation with hg(ii). Appl. Geochem. 22 (8), 1668–1679.

Haag, W.R., Hoigné, J., 1985. Photo-sensitized oxidation in natural water via .Oh radicals. Chemosphere 14 (11), 1659–1671.

Haag, W.R., Hoigne´, J.r., Gassman, E., Braun, A.M., 1984. Singlet oxygen in surface waters — part i: furfuryl alcohol as a trapping agent. Chemosphere 13 (5), 631–640.

Hansen, A.M., Kraus, T.E.C., Pellerin, B.A., Fleck, J.A., Downing, B.D., Bergamaschi, B.A., 2016. Optical properties of dissolved organic matter (dom): effects of biological and photolytic degradation. Limnol. Oceanogr. 61 (3), 1015–1032.

Helms, J.R., Stubbins, A., Ritchie, J.D., Minor, E.C., Kieber, D.J., Mopper, K., 2008. Absorption spectral slopes and slope ratios as indicators of molecular weight, source, and photobleaching of chromophoric dissolved organic matter. Limnol. Oceanogr. 53 (3), 955–969.

Hong, H., Wu, J., Shang, S., Hu, C., 2005. Absorption and fluorescence of chromophoric dissolved organic matter in the pearl river estuary, south china. Mar. Chem. 97 (1), 78–89.

Huguet, A., Vacher, L., Relexans, S., Saubusse, S., Froidefond, J.M., Parlanti, E., 2009. Properties of fluorescent dissolved organic matter in the gironde estuary. Org. Geochem. 40 (6), 706–719.

Kothawala, D.N., Stedmon, C.A., Müller, R.A., Weyhenmeyer, G.A., Köhler, S.J., Tranvik, L.J., 2014. Controls of dissolved organic matter quality: evidence from a large-scale boreal lake survey. Global Change Biol. 20 (4), 1101–1114.

Laszakovits, J.R., Berg, S.M., Anderson, B.G., O'Brien, J.E., Wammer, K.H., Sharpless, C. M., 2017. P-nitroanisole/pyridine and p-nitroacetophenone/pyridine actinometers revisited: quantum yield in comparison to ferrioxalate. Environmental Science & Technology Letters 4 (1), 11–14.

Lee, E., Glover, C.M., Rosario-Ortiz, F.L., 2013. Photochemical formation of hydroxyl radical from effluent organic matter: role of composition. Environ. Sci. Technol. 47 (21), 12073–12080.

Maizel, A.C., Li, J., Remucal, C.K., 2017. Relationships between dissolved organic matter composition and photochemistry in lakes of diverse trophic status. Environ. Sci. Technol. 51 (17), 9624–9632.

Maizel, A.C., Remucal, C.K., 2017a. The effect of probe choice and solution conditions on the apparent photoreactivity of dissolved organic matter. Environmental Science: Processes & Impacts 19 (8), 1040–1050.

Maizel, A.C., Remucal, C.K., 2017b. Molecular composition and photochemical reactivity of size-fractionated dissolved organic matter. Environ. Sci. Technol. 51 (4), 2113–2123.

McCabe, A.J., Arnold, W.A., 2016. Seasonal and spatial variabilities in the water chemistry of prairie pothole wetlands influence the photoproduction of reactive intermediates. Chemosphere 155, 640–647.

McKay, G., Huang, W., Romera-Castillo, C., Crouch, J.E., Rosario-Ortiz, F.L., Jaffé, R., 2017. Predicting reactive intermediate quantum yields from dissolved organic matter photolysis using optical properties and antioxidant capacity. Environ. Sci. Technol. 51 (10), 5404–5413.

McKnight, D.M., Boyer, E.W., Westerhoff, P.K., Doran, P.T., Kulbe, T., Andersen, D.T., 2001. Spectrofluorometric characterization of dissolved organic matter for indication of precursor organic material and aromaticity. Limnol. Oceanogr. 46 (1), 38–48.

Meng, F., Huang, G., Yang, X., Li, Z., Li, J., Cao, J., Wang, Z., Sun, L., 2013. Identifying the sources and fate of anthropogenically impacted dissolved organic matter (dom) in urbanized rivers. Water Res. 47 (14), 5027–5039.

Mostafa, S., Rosario-Ortiz, F.L., 2013. Singlet oxygen formation from wastewater organic matter. Environ. Sci. Technol. 47 (15), 8179–8186.

Murphy, K.R., Hambly, A., Singh, S., Henderson, R.K., Baker, A., Stuetz, R., Khan, S.J., 2011. Organic matter fluorescence in municipal water recycling schemes: toward a unified parafac model. Environ. Sci. Technol. 45 (7), 2909–2916.

Murphy, K.R., Stedmon, C.A., Graeber, D., Bro, R., 2013. Fluorescence spectroscopy and multi-way techniques. Parafac. Analytical Methods. 5 (23), 6557–6566.

Murphy, K.R., Stedmon, C.A., Waite, T.D., Ruiz, G.M., 2008. Distinguishing between terrestrial and autochthonous organic matter sources in marine environments using fluorescence spectroscopy. Mar. Chem. 108 (1), 40–58.

Murphy, K.R., Stedmon, C.A., Wenig, P., Bro, R., 2014. Openfluor– an online spectral library of auto-fluorescence by organic compounds in the environment. Anal. Methods 6 (3), 658–661.

Ni, M., jiang, S., Li, S., 2020. Spectroscopic indices trace spatiotemporal variability of dissolved organic matter in a river system with karst characteristic. J. Hydrol. 590, 125570.

Niu, X.-Z., Liu, C., Gutierrez, L., Croué, J.-P., 2014. Photobleaching-induced changes in photosensitizing properties of dissolved organic matter. Water Res. 66, 140–148.

O'Connor, M., Helal, S.R., Latch, D.E., Arnold, W.A., 2019. Quantifying photo-production of triplet excited states and singlet oxygen from effluent organic matter. Water Res. 156, 23–33.

Page, S.E., Arnold, W.A., McNeill, K., 2010. Terephthalate as a probe for photochemically generated hydroxyl radical. J. Environ. Monit. 12 (9), 1658–1665.

Page, S.E., Arnold, W.A., McNeill, K., 2011. Assessing the contribution of free hydroxyl radical in organic matter-sensitized photohydroxylation reactions. Environ. Sci. Technol. 45 (7), 2818–2825.

Page, S.E., Logan, J.R., Cory, R.M., McNeill, K., 2014. Evidence for dissolved organic matter as the primary source and sink of photochemically produced hydroxyl radical in arctic surface waters. Environmental Science: Processes & Impacts 16 (4), 807–822.

Peterson, B.M., McNally, A.M., Cory, R.M., Thoemke, J.D., Cotner, J.B., McNeill, K., 2012. Spatial and temporal distribution of singlet oxygen in lake superior. Environ. Sci. Technol. 46 (13), 7222–7229.

Sharpless, C.M., Blough, N.V., 2014. The importance of charge-transfer interactions in determining chromophoric dissolved organic matter (cdom) optical and photochemical properties. Environmental Science: Processes & Impacts 16 (4), 654–671.

Spencer, R.G.M., Aiken, G.R., Wickland, K.P., Striegl, R.G., Hernes, P.J., 2008. Seasonal and spatial variability in dissolved organic matter quantity and composition from the yukon river basin. Alaska. Global Biogeochemical Cycles. 22 (4), GB4002.

Stedmon, C.A., Bro, R., 2008. Characterizing dissolved organic matter fluorescence with parallel factor analysis: a tutorial. Limnology and Oceanography: Methods 6 (11), 572–579.

Sulzberger, B., Arey, J.S., 2016. Impacts of polar changes on the uv-induced mineralization of terrigenous dissolved organic matter. Environ. Sci. Technol. 50 (13), 6621–6631.

Timko, S.A., Romera-Castillo, C., Jaffé, R., Cooper, W.J., 2014. Photo-reactivity of natural dissolved organic matter from fresh to marine waters in the florida everglades, usa. Environmental Science: Processes & Impacts. 16 (4), 866–878.

Vione, D., Falletti, G., Maurino, V., Minero, C., Pelizzetti, E., Malandrino, M., Ajassa, R., Olariu, R.-I., Arsene, C., 2006. Sources and sinks of hydroxyl radicals upon irradiation of natural water samples. Environ. Sci. Technol. 40 (12), 3775–3781.

Vione, D., Minella, M., Maurino, V., Minero, C., 2014. Indirect photochemistry in sunlit surface waters: photoinduced production of reactive transient species. Chemistry – A European Journal. 20 (34), 10590–10606.

Wan, D., Sharma, V.K., Liu, L., Zuo, Y., Chen, Y., 2019. Mechanistic insight into the effect of metal ions on photogeneration of reactive species from dissolved organic matter. Environ. Sci. Technol. 53 (10), 5778–5786.

Wasswa, J., Driscoll, C.T., Zeng, T., 2020. Photochemical characterization of surface waters from lakes in the adirondack region of new york. Environ. Sci. Technol. 54 (17), 10654–10667.

Wold, S., Sjöström, M., Eriksson, L., 2001. Pls-regression: a basic tool of chemometrics. Chemom. Intell. Lab. Syst. 58 (2), 109–130.

Xu, H., Li, Y., Liu, J., Du, H., Du, Y., Su, Y., Jiang, H., 2020. Photogeneration and steady-state concentration of hydroxyl radical in river and lake waters along middle-lower yangtze region, china. Water Res. 176, 115774.

Yamashita, Y., Jaffé, R., 2008. Characterizing the interactions between trace metals and dissolved organic matter using excitation−emission matrix and parallel factor analysis. Environ. Sci. Technol. 42 (19), 7374–7379.

Zeng, T., Arnold, W.A., 2013. Pesticide photolysis in prairie potholes: probing photosensitized processes. Environ. Sci. Technol. 47 (13), 6735–6745.

Zhang, D., Yan, S., Song, W., 2014. Photochemically induced formation of reactive oxygen species (ros) from effluent organic matter. Environ. Sci. Technol. 48 (21), 12645–12653.

Zhou, H., Yan, S., Lian, L., Song, W., 2019. Triplet-state photochemistry of dissolved organic matter: triplet-state energy distribution and surface electric charge conditions. Environ. Sci. Technol. 53 (5), 2482–2490.